Effect of Carbon Dioxide on the Degradation of Chemical Warfare Agent Simulant in the Presence of Zr Metal Organic Framework MOF-808

Anna M. Plonka,[†] Tyler G. Grissom,[‡] Djamaladdin G. Musaev,[§,||] Alex Balboa,[⊥] Wesley O. Gordon,[⊥] Daniel L. Collins-Wildman,[||] Sanjit K. Ghose,[#] Yiyao Tian,[†] Amani M. Ebrahim,[†] Mark B. Mitchell,[g] Craig L. Hill,[||] John R. Morris,[‡] and Anatoly I. Frenkel*,[†,h]

[†]Department of Materials Science and Chemical Engineering, Stony Brook University, Stony Brook, New York 11794, United States

[‡]Department of Chemistry, Virginia Tech, Blacksburg, Virginia 24061, United States

[§]Cherry L. Emerson Center for Scientific Computation, Emory University, Atlanta, Georgia 30322, United States

[||]Department of Chemistry, Emory University, Atlanta, Georgia 30322, United States

[⊥]U.S. Army CCDC Chemical Biological Center, APG, Aberdeen Proving Ground, Maryland 21010, United States

[#]National Synchrotron Light Source II, Brookhaven National Laboratory, PO Box 5000, Upton, New York 11973, United States

[g]Department of Chemistry, Kennesaw State University, Kennesaw, Georgia 30144, United States

[h]Division of Chemistry, Brookhaven National Laboratory, Upton, New York 11794, United States

S *Supporting Information*

ABSTRACT: Developing novel and more efficient filters for chemical warfare agent (CWA) decomposition remains an important challenge for modern technology due to the continuous threat those weapons present in the event of use. Recently, metal−organic frameworks (MOFs) have attracted attention as potential catalysts for nerve agent decomposition. However, in order to improve their performance under battlefield conditions, it is crucial to understand the influence of ambient contaminants such as carbon dioxide on CWA adsorption and decomposition. Here, we present a comprehensive experimental and computational study on the influence of CO_2 on the adsorption and decomposition of the CWA simulant dimethyl methyl phosphonate (DMMP) by the Zr-based MOF-808. The study combined in situ synchrotron powder X-ray diffraction (PXRD) with variable-temperature infrared spectroscopy (VTIR) and computations. PXRD and experiments with pure CO_2 revealed that the MOF framework contracts by 0.2% after CO_2 saturation and CO_2 adsorbs within the MOF-808 framework via dispersion forces with an enthalpy of adsorption of -32.2 ± 1.8 kJ/mol. From five DRIFTS experiments conducted in various gas flow regimes we established that CO_2 interferes with the decomposition of DMMP due to the formation of carbonate species, while if it is used as a regeneration agent, it accelerates the desorption of DMMP and DMMP decomposition products. In situ PXRD experiments showed that CO_2 also limited expansion of the framework due to the formation of carbonate species by 40% in comparison to values in a control experiment with N_2. The main conclusions of the computational study are (a) CO_2 reversibly adsorbs onto MOF-808 via both μ_3-OH groups located within the tetrahedral pores of the MOF and/or to the MOF surface with stabilizing dispersion interactions, (b) the presence of DMMP provides stability to the $CO_2-(\mu_3$-OH) moiety, which hinders the μ_3-OH transfer to the DMMP molecule required for the nerve-agent decomposition until the carbonyl to carbonate transformation is completed, and (c) CO_2 molecules are not sufficient for the regeneration of the MOF when DMMP decomposition products are present but rather there is desorption of bound DMMP.
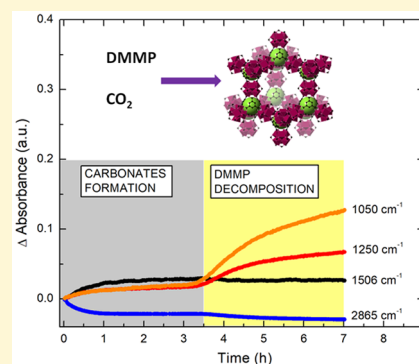
INTRODUCTION

Chemical warfare agents (CWAs) are extremely toxic chemicals that are public health concerns and that have been used in the past by terrorist groups and in large- and small-scale warfare.[1] Thus, the development of efficient methods for the capture and destruction of CWAs in the battlefield and under noncombat conditions remains a crucial task and continues to be of major national security interest.[1−3]

Currently, the detoxification of CWAs is performed via photocatalytic[4] and incineration methods,[5,6] as well as the use of strong oxidants,[7] enzymatic biodegradation processes,[8] or atmospheric pressure plasma.[9] These methods present

significant drawbacks, including the lack of stability that leads to loss of activity over time, strong environmental impact, and high temperature requirements, which make them unsuitable for large-scale field-based detoxification of CWAs. The development of new environmentally friendly and cost-effective strategies for decontamination of CWAs is thus necessary.

Two main types of CWAs include G-type nerve agents such as sarin, soman, and tabun and vesicants such as mustard gas (sulfur mustard).[10,11] Nerve agents affect signal transmission from the nervous system to the muscles, causing incapacitation.[9] These agents are organophosphorus compounds, each containing P−X bonds, where X is a leaving group such as F or CN.[3] In general, nerve agents are degraded through general base hydrolysis, where the P−X bond is broken, leading to the formation of less toxic byproducts such as methylphosphonic acid and methanol.[3] Although G-type nerve agents are soluble in and decompose in water, the reactions involving metal catalysts significantly accelerate the decomposition process.[3] The development of novel solid-state materials with active metal centers, catalytically reactive with gaseous CWAs, is needed for nerve-agent decontamination, specifically when CWAs are delivered in the vapor phase. These challenges have motivated research into a new generation of sorptive or catalytically active materials for CWA decontamination, including metal oxides and hydroxides,[3,12,13] polyoxometalates (POMs),[10,14,15] zeolites,[16] organic polymers,[17] and metal−organic frameworks (MOFs).[18−37]

MOFs are a class of hybrid materials consisting of metal atoms or atom clusters connected by organic ligands that form extensive frameworks in one, two, or three dimensions. Some of those frameworks retain their porosity after solvent removal, enabling the formation of materials with high porosity and ultrahigh surface areas.[38] Due to their porous nature, MOFs have possible applications in areas such as gas storage,[39] gas separation,[40] sensing,[38] catalysis,[41,42] and toxics filtration,[43] including catalytic decontamination of CWAs.[18−36] Zirconium-based MOFs have been the most extensively studied for the catalytic decomposition of CWAs because of their water stability and high thermal stability.[44] In one of the first reports on the subject, Farha, Hupp, et al. studied the Zr-based MOF NU-1000 and identified that it was able to efficiently capture and degrade, by catalytic hydrolysis, the nerve agent soman.[32] Further, Katz et al. and Kalaj et al. investigated CWA simulant decontamination in a series of pristine and functionalized UiO-66 and UiO-67 and discovered that the amino and bromine derivatives of UiO MOFs are more active for CWA decomposition in comparison to nonfunctionalized materials.[45,46] Liu et al. identified a porphyrin-based Zr(IV) MOF (PCN-222) to be a dual-function catalyst for the simultaneous decomposition of two different CWA simulants at room temperature.[47]

Despite promising preliminary research on Zr(IV) MOFs, there is a further need to determine the effect of atmospheric components such as H_2O and CO_2 on the reactions of MOFs with CWAs. CO_2 is an important component of detoxification efforts both in the battlefield and under noncombat conditions due to elevated levels in personal protective equipment such as gas masks or hazardous materials suits. Studies performed under pristine laboratory conditions can have dramatically different results from operations in relevant battlefield environments. The disparities can include unexpected decomposition performance, lowered dependability, or com-

plications with deployment methods.[48] Pehrsson and co-workers studied the environmental effects on $Zr(OH)_4$—a well-known sorbent for CWA detoxification—and found that elevated humidity promoted hydrolysis of the adsorbed simulant but high concentrations of CO_2 reduced decomposition kinetics. In another study on solid-state CWA decomposition catalysts, Musaev and co-workers similarly observed that CO_2 shields the active sites of the polyoxoniobates and hinders the hydrolysis reaction.[49] In the case of Zr(IV) MOFs, we have previously shown that Zr(IV) MOFs are effective at the removal of CWA simulants from the air.[33] Further, Ryu et al. and Cho et al. reported that UiO MOFs maintain nerve agent decomposition ability, both under high relative humidity and in water,[24,37] but the detailed influence of CO_2 on CWA detoxification has not been reported to date.

In this work, we combined in situ synchrotron X-ray diffraction with in situ IR spectroscopy and theoretical calculations to take a detailed look at the CO_2 and MOF-808 interaction and the influence of CO_2 on MOF-808 performance for CWA decomposition. MOF-808 is a porous framework constructed of hexazirconium(IV) nodes, with the general formula $Zr_6(\mu_3\text{-}O)_4(\mu_3\text{-}OH)_4(HCOO)_6(OH)_6(H_2O)_6$, connected with 1,3,5-benzenetricarboxylate linkers (Figure 1).[44] The framework contains two types of pores: smaller
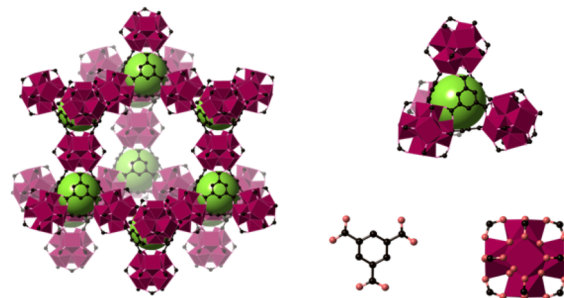

Figure 1. Structure of MOF-808. $Zr_6(\mu_3\text{-}O)_4(\mu_3\text{-}OH)_4(HCOO)_6(OH)_6(H_2O)_6$ metal clusters (purple) and a 1,3,5-benzenetricarboxylate linker form tetrahedral cages (green spheres represent the internal free volume of 4.8 Å) and large adamantane-shaped cages of 18 Å.

tetrahedral cages with an internal free diameter of 4.8 Å and large adamantane-shaped cages with a diameter of 18 Å.[50] The larger pores and pore opening ensure the fast delivery of the nerve agents or nerve agent simulants inside the framework, which are advantageous characteristics in the development of sorbent materials for rapid CWA hydrolysis.[33] MOF-808 is an excellent candidate for these studies, since it was reported to display the highest CWA simulant hydrolysis rates among all Zr-MOFs.[32] In our experiments, we used dimethyl methyl phosphonate (DMMP) as a nerve agent simulant, which has a structural similarity to sarin (Figure S1) but has the advantage of significantly lower toxicity.[51]

MATERIALS AND METHODS

Synthesis of the Sample. The preparation of MOF-808 was modified from the reported literature method.[50] Typically, 1,3,5-benzenetricarboxylic acid (H_3btc, 0.11 g, 0.50 mmol) and $ZrOCl_2 \cdot 8H_2O$ (0.16 g, 0.50 mmol) were added to a mixed solvent of dimethylformamide (DMF) and formic acid (20 mL/20 mL). The mixture was then stirred for 30 min and transferred to an autoclave, which was heated at 373 K for 7 days. White crystalline powders were

collected by centrifugation and washed extensively with DMF and anhydrous acetone. The obtained materials were further vacuum-dried at 423 K for 8 h.

In Situ X-ray Diffraction (XRD) Measurements. For time-resolved in situ X-ray diffraction, the MOF-808 sample was loaded into a Kapton capillary of 1.15 mm outside diameter. Both ends of the capillary were loaded with quartz wool to immobilize the sample while allowing the gas to flow through. The capillary was attached to the flow cell with Swagelock fittings and graphite ferrules. The input of the cell was connected to a gas inlet system that carried gas to the cell. The outlet was connected to a trap and released to exhaust. During the experiment the gas flow rate was fixed at 10 mL/min and controlled with the mass flow controller. A total of four in situ experiments were performed: two pure CO_2 and N_2 adsorption/desorption experiments and two DMMP-doses in the N_2 and CO_2 carrier gases. At the beginning of each experiment samples were desolvated (activated) in situ using a He gas flow for 2 h at 383 K. After it was cooled to room temperature, the MOF sample was exposed to the flowing gases of interest. The X-ray diffraction experiments involving pure N_2 and CO_2 adsorption and desorption in He were performed with synchrotron X-rays at the 17-BM beamline at the Advanced Photon Source (APS) at Argonne National Laboratory with the PerkinElmer amorphous silicon 2D detector, using a monochromatic beam of $\lambda = 0.72959$ Å, and were analyzed using GSAS-II software.[52] The NIST standard LaB_6 was used for calibration of the detector geometry in the transmission mode.

For the time-resolved in situ X-ray diffraction experiment of DMMP dosing the input of the cell was connected to a gas inlet system that carried DMMP vapor with N_2 or CO_2 to the cell. During the dosing stage of the experiment carrier gas was flowing through a fritted glass saturator filled with DMMP (~5 mL) liquid kept at ~313 K using a water bath. In order to avoid condensation of DMMP vapors, the carrier lines were also heated to 343 K using heating tapes. After activation and cooling to room temperature, the MOF samples were exposed to DMMP for 2 h. In situ PXRD data were collected every 1 min during the whole experiment, including activation and DMMP treatment. The powder XRD diffraction data were collected at the X-ray Powder Diffraction (XPD) beamline of the National Synchrotron Light Source-II, Brookhaven National Laboratory, using a monochromatic beam of $\lambda = 0.29411$ Å. Diffraction data were collected in transmission mode with an amorphous silicon-based flat panel detector (PerkinElmer), mounted orthogonal to and centered on the beam path, and were analyzed with the Fit2D software.[53] The NIST standard LaB_6 was used for calibration of the detector geometry.

The model of the empty framework structure of MOF-808 was refined on the basis of the previously published structure[44] with the Rietveld method,[54] using the Jana2006[55] software. The difference electron density map of the CO_2-loaded MOF was calculated using the refined framework structure. The unit cell parameters of MOF-808 in all four experiments were obtained from initial Le Bail fitting, where the peak shape was refined with a pseudo-Voigt function and peak asymmetry corrected with a Simpson function.[55] The background was modeled manually using 50 points. The structure of DMMP-loaded MOF-808 could not be refined, due to significant disorder of DMMP molecules.[56] During the Rietveld refinement of the initial MOF-808 structure 16 soft distance restraints were used. The atomic coordinates and isotropic atomic displacement parameters for all framework atoms were refined; hydrogen atoms were added to the linker moieties using riding commands.

Variable-Temperature Infrared Spectroscopy (VTIR). The sample preparation was adapted from the method reported by Grissom et al.[57] Briefly, MOF-808 was pressed into a 50 μm thick tungsten mesh (Tech Etch) and mounted onto a nickel support clamp containing copper power leads. K-type thermocouples were spot-welded onto the mesh adjacent to the pressed sample, which allowed for real-time temperature monitoring. The power leads were connected to a sample manipulator and terminated at an external power supply, which allowed for precise control of the sample temperature through resistive heating. The sample manipulator was placed onto a custom-built vacuum chamber, and gases were evacuated from the chamber until a base pressure below 5×10^{-8} Torr was reached. Operation under high-vacuum conditions keeps the sample clean and allows for the probing of gas–MOF interactions free of ambient or contaminant gas contributions. The VTIR method has been reported previously.[58] Briefly, the MOF-808 sample was thermally activated by heating at 448 K for 3 h under vacuum to remove loosely-bound water collected during storage. The interactions that take place between CO_2 and MOF-808 was investigated by back-filling the vacuum chamber with 1.5 Torr of CO_2. An IR spectrum was collected at 303 K (Figure S2). Fourier-transform infrared (FTIR) spectra of MOF-808 + CO_2 were then collected at a series of temperatures ranging from 303 to 383 K.

In Situ Diffuse Reflectance Infrared Fourier Transform Spectroscopy (DRIFTS). DRIFTS data were collected with a Thermo Scientific Nicolet iS50 FT-IR spectrometer using an MCT/A detector. A Harrick cell was used for the in situ experiments. In the case of each in situ experiment the first step involved activation (desolvation) of the sample and each experiment was performed in the same fashion. First, approximately 20 mg of the sample was loaded into the Harrick cell with 10 mL/min of He flow (regulated with a Brooks Instruments mass flow controller). The temperature was gradually increased to 383 K, and the sample was at 383 K for 18 h. After activation was completed, the sample was cooled to 298 K and the spectra were collected. Single-beam spectra collected after activation were later used as a background in the in situ DMMP dosing/desorption experiments. In DRIFTS experiments, the same sequence of experiments as with XRD was used. During absorption experiments, the input of the cell was connected to a gas inlet system that carried DMMP vapor with carrier gas mixture to the cell. Carrier gas was flowing through the saturator filled with DMMP liquid (1−5 mL) kept at a temperature of 313 K in a water bath. The lines that delivered DMMP vapors to the cell were heated to 313 K. In situ DRIFTS data were collected in continuous mode (128 scan spectra; 58 s per spectrum) during the whole experiment.

A total of five in situ experiments were performed. In the first two experiments N_2 and CO_2 were used as carrier gases for DMMP; the objective of the study was to compare the N_2 and CO_2 influence on the mechanism and rate of DMMP decomposition. After activation the sample was exposed to the DMMP/N_2 or DMMP/CO_2 at a rate of 10 mL/min. During the third experiment CO_2 was again used as the carrier gas for DMMP but the flow rate was increased to 50 mL/min rate in order to accelerate the reaction.

Two additional experiments were performed to examine the effect of the carrier gas on DMMP desorption from fully loaded MOF-808 with a He or CO_2 flow. The dosing part of the experiment was performed identically during both experiments, where the sample was exposed to DMMP in He carrier gas for 24 h at a flow rate of 10 mL/min. Then the gas was switched to pure He or CO_2 for 24 h with a 10 mL/min flow rate. The last step involved heating the sample to activation temperature (383 K) in He flow.

As a control for the DMMP experiment we performed two DRIFTS experiments with CO_2 and H_2O. Before the experiments MOF-808 samples were activated at 383 K for 18 h. In the first experiment MOF-808 sample was exposed to a He/CO_2/H_2O mixture, with 20% CO_2 and 10% H_2O (40% relative humidity). In the second experiment the MOF-808 sample was exposed to 100% CO_2 for 30 min and then to a He/H_2O mixture (100% relative humidity) for 30 min.

Computational Methodology. All presented calculations were carried out with the M06-L density functional,[59] as implemented in the Gaussian09 code.[60] Here we used 6-31G(d,p) basis sets for C, H, O, and P and Lanl2dz basis sets with corresponding Hay–Wadt effective core potentials for Zr.[61,62] The reported structures were confirmed to have all real frequencies (minima). The reported gas-phase enthalpies and Gibbs free energies are computed at a temperature of 298.15 K and pressure of 1 atm.
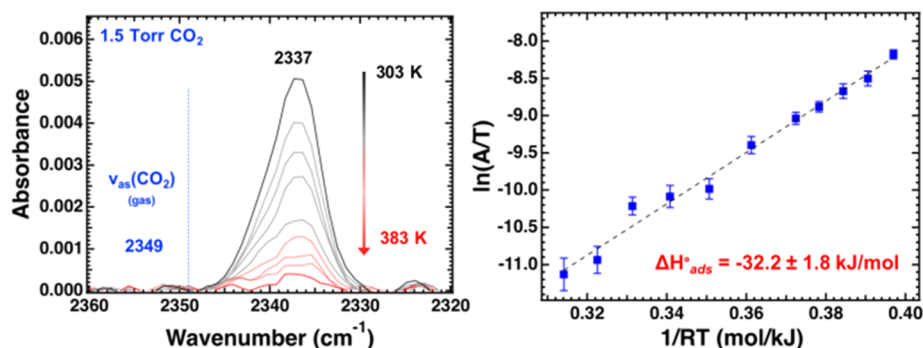
Figure 2. CO_2 on MOF-808 between 303 and 383 K: (a) infrared spectra of the $\nu_{as}(CO_2)$ mode of adsorbed CO_2 (black to red) under 1.5 Torr CO_2 and (blue dashed line) the location of the fundamental frequency of gas-phase CO_2; (b) van't Hoff plot, where the slope of the best-fit line gives the value of $\Delta H°_{ads}$.

■ RESULTS AND DISCUSSION

CO_2 Interaction with MOF-808. Metal−organic frameworks have been reported previously to interact with gaseous CO_2.[39] We have employed high-vacuum (HV)-based infrared spectroscopic methods and in situ powder X-ray diffraction (PXRD) to characterize the energetics and mechanism of interaction between CO_2 and MOF-808 prior to exposure to DMMP. In the HV-IR study the only observed change after the exposure to CO_2 was the formation of a feature at 2337 cm^{-1}, which is associated with the $\nu_{as}(CO_2)$ signal of adsorbed CO_2 stabilized by dispersion forces.[58] This feature was found to decrease with increasing temperature (Figure 2). Collection of IR spectra over a range of temperatures provides insight into the energetics of CO_2 adsorption by use of a van't Hoff analysis which relates the equilibrium constant, K_{eq}, to the standard enthalpy of adsorption, $\Delta H°_{ads}$,[63] as shown in eq 1

$$\ln K_{eq} = \left(\frac{-\Delta H°_{ads}}{RT}\right)\left(\frac{\Delta S°_{ads}}{R}\right) \qquad (1)$$

where $\Delta S°ads$ is the standard entropy of adsorption, R is the gas constant, and T is the temperature. Using the assumption that the CO_2 coverage on the MOF is low, the gas-phase concentration is high, and $\Delta H°ads$ is constant over the temperature range examined, the integrated absorbance, A, at each temperature can be related to the $\Delta H°_{ads}$ by eq 2.

$$\ln \frac{A}{T} \propto \frac{-\Delta H°_{ads}}{RT} \qquad (2)$$

The results of the van't Hoff analysis of CO_2 adsorption on MOF-808 are presented in Figure 2. As expected, the amount of adsorbed CO_2, on the basis of the area of the $\nu_{as}(CO_2)$ feature at 2337 cm^{-1}, decreased as the sample temperature increased. The slope of the van't Hoff plot in Figure 2b reveals the $\Delta H°_{ads}$ value of CO_2 on MOF-808 to be −32.2 ± 1.8 kJ/mol, consistent with CO_2 adsorption enthalpies found in other zirconium- or benzenecarboxylate-based MOFs.[39,58,64,65] Upon evacuation of CO_2 from the vacuum chamber, the adsorbed CO_2 was immediately removed at 303 K, and the IR spectrum of the MOF returned to the original, pre-CO_2 exposed state.

We performed in situ powder X-ray diffraction to better understand the effect CO_2 has on the MOF and to locate the main CO_2 adsorption sites. Exposure to CO_2 at 300 K does not dramatically change the powder diffraction pattern, indicating that the MOF topology (Figure 1) is preserved. The small changes (Figure S4) do indicate, however, that CO_2 was indeed adsorbed within the pore space of MOF-808. After a

switch from CO_2 to He gas, the changes reverse (Figure S4), suggesting that CO_2 desorbs quickly, in agreement with the IR results. Exposure to N_2 (at room temperature) does not lead to any changes in the PXRD (Figure S5) most probably due to an insignificant uptake of N_2.[66] The Le Bail fit further revealed that, upon CO_2 exposure, the framework contracted with a maximum unit cell volume change of −0.2% at 300 K, consistent with the previously reported CO_2−framework interactions, where the introduction of CO_2 or other strongly interacting small molecules leads to the contraction of the pores.[67]

Beyond structural changes to the MOF, the PXRD data provide insight into the location of adsorbed CO_2 via Fourier difference analysis of the empty and CO_2-loaded frameworks. The starting structural model for MOF-808 was refined with the Rietveld method from the data acquired from the activated sample in He. Rietveld refinement of the CO_2-loaded MOF-808 confirmed that the structure is retained and no significant breathing or reorganization was observed. The residual electron density inside the pores that cannot be assigned to the framework atoms was identified as adsorbed CO_2 molecules with predominant localization in close proximity to benzenetricarboxylate linkers inside the tetrahedral pores (Figure 3). Adsorbed CO_2 molecules presumably interact with MOF-808 through dispersion forces.[39] Such an interaction is consistent with the −32.2 ± 1.8 kJ/mol enthalpy of CO_2 obtained from IR experiments.[65]

CO_2 Influence on the Reaction with DMMP. The effect of CO_2 on the MOF-808 interaction with DMMP was studied with in situ DRIFTS and in situ synchrotron PXRD; for the control experiments we used N_2 as a carrier gas. The powder diffraction experiments show significant changes upon exposure to DMMP as opposed to pure N_2 or CO_2. Examination of the collected patterns clearly reveals that the sample undergoes structural changes during DMMP adsorption, in agreement with previously reported results.[33] The most apparent change is the decrease in intensity of the low-angle reflection relative to higher-angle reflections. This behavior is typically indicative of adsorbates entering porous materials, which suggests that DMMP diffused into the pore space of MOF-808 during exposure.

Apart from changes in the peak intensity, we observed that exposure to DMMP shifts reflections toward lower 2θ angles, indicating the expansion of the lattice. Results from Le Bail analysis show that in the case of N_2 the unit cell started expanding approximately 20 min after the start of the experiment and the expansion was finalized at approximately
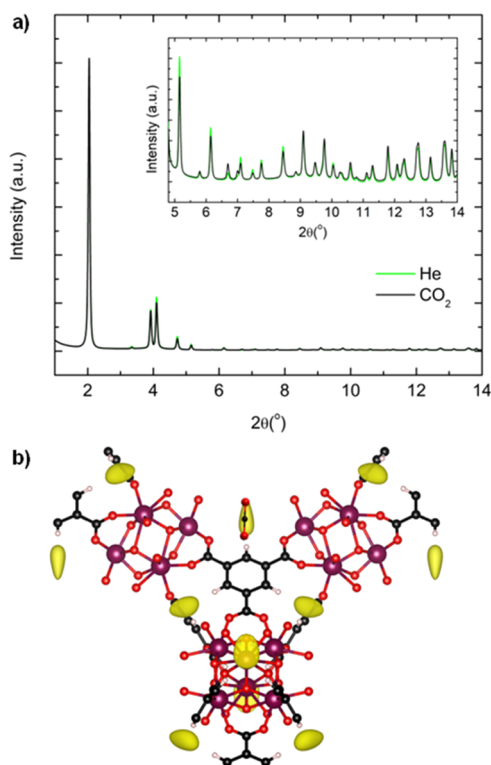
Figure 3. Results of the in situ PXRD experiment. (a) Difference Fourier electron density map of MOF-808 with adsorbed CO_2 (right) calculated from in situ PXRD data (left). (b) Residual electron density isosurface drawn at 0.2 e/Å^3 in yellow. The overlaid CO_2 molecule shows the suggested position. Color code: Zr, purple; O, red; C, black; H, white.

60 min with a maximum increase of 1.2% in lattice volume. When CO_2 was used as a carrier gas, the expansion of the unit cell started instantaneously and reached a maximum of 0.7% of the initial volume in 15 min and no further increase was observed (Figure 4). The difference in the behavior of the MOF-808 framework can be explained by the formation of carbonate species when the DMMP was introduced to MOF-
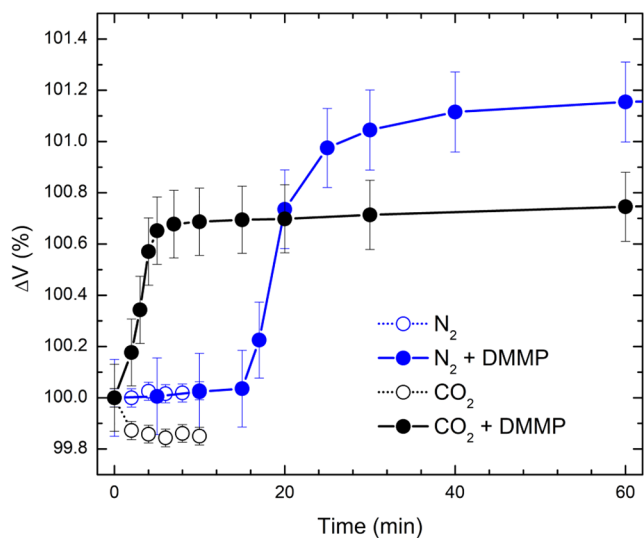

Figure 4. Evolution of MOF-808 unit cell volume with the dosing of DMMP and pure carrier gases.

808 together with CO_2, as revealed by DRIFTS measurements (vide infra).

To evaluate the fate of DMMP within the pores of MOF-808 in the presence of CO_2 and to characterize reaction products, we performed in situ DRIFTS measurements. In the first group of experiments, we used a 10 mL/min gas flow of CO_2 or N_2 (control) carrying DMMP into the cell with the activated MOF-808. The IR spectra were collected continuously over time during dynamic adsorption of DMMP by the MOF and are plotted in Figure 5 and Figures S6 and S7.
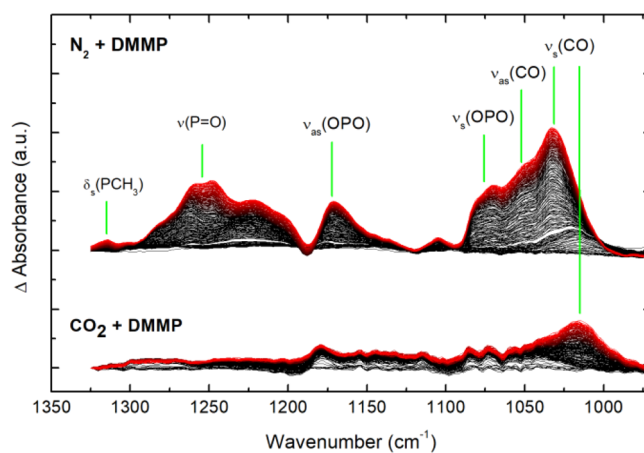

Figure 5. Fingerprint region of the background-corrected in situ difference DRIFTS spectra collected over 7 h during a DMMP adsorption experiment with N_2 or CO_2 carrier gas (flow rate 10 mL/min).

When N_2 was used as a carrier gas for DMMP, we observed the formation of absorption bands consistent with physisorption and decomposition of DMMP to produce methyl methylphosphonic acid (MMPA), showing that N_2 behaves similarly to He; hence, N_2 does not appear to influence the DMMP−MOF interaction.[33] Upon exposure to DMMP, we observed the appearance of new IR bands, which can be assigned to the adsorbed DMMP. The differential spectra also show a negative feature at 3668 cm^{-1} (Figure S6) assigned to the free OH stretching vibration, which indicates the formation of hydrogen bonds between the guest DMMP and hydroxyl groups at the inorganic nodes. The consumption of free hydroxyl groups is also indicative of the hydrolysis of DMMP to form MMPA.[19] Further, the appearance of many new bands in the low-wavenumber region between 1000 and 1350 cm^{-1}, consistent with previous reports of both gaseous and adsorbed DMMP, support the physisorption/decomposition of DMMP inside the MOF-808 pores.[19,37] In that region, adsorbed DMMP is indicated by the $\nu(P{=}O)$ band at 1250 cm^{-1} (Figure 5). Peaks indicating DMMP hydrolysis to the bridging MMPA species are seen at 1030, 1050, 1065, 1170, and 1312 cm^{-1}, which are assigned to the $\nu_s(CO)$, $\nu_a(CO)$, $\nu_s(OPO)$, $\nu_a(OPO)$, and $\rho(PCH_3)$ modes of DMMP byproducts on the surface, respectively (Figure 5).[19,37]

In the case of CO_2, during the same time frame of the reaction no significant peaks from DMMP/MMPA are observed, indicating that CO_2 hinders DMMP adsorption and decomposition. The only significant band present in the fingerprint region can be assigned as $\nu_s(CO)$. Further, we can see the formation of the carbonate species, as evidenced by the growth of the $\nu_{as}(CO_3)$ mode at 1506 cm^{-1} and the

consumption of hydroxyl groups, which is evidenced by a negative-going IR feature at 3670 cm^{-1} (Figure S7).

In order to accelerate the reaction, we performed a second experiment where the CO_2 carrier gas flow was increased by a factor of 5 to 50 mL/min. Here, the results indicate that the reaction has two steps—in the first 3 h we observe very slow growth of DMMP-related modes, while carbonate species are forming quickly, as evidenced by the fast growth of the $\nu_{as}(CO_3)$ mode at 1506 cm^{-1}. Once the carbonate formation is finished, where presumably all sites within the MOF-808 framework are occupied, fast growth of DMMP and MMPA modes is observed (Figure 6).
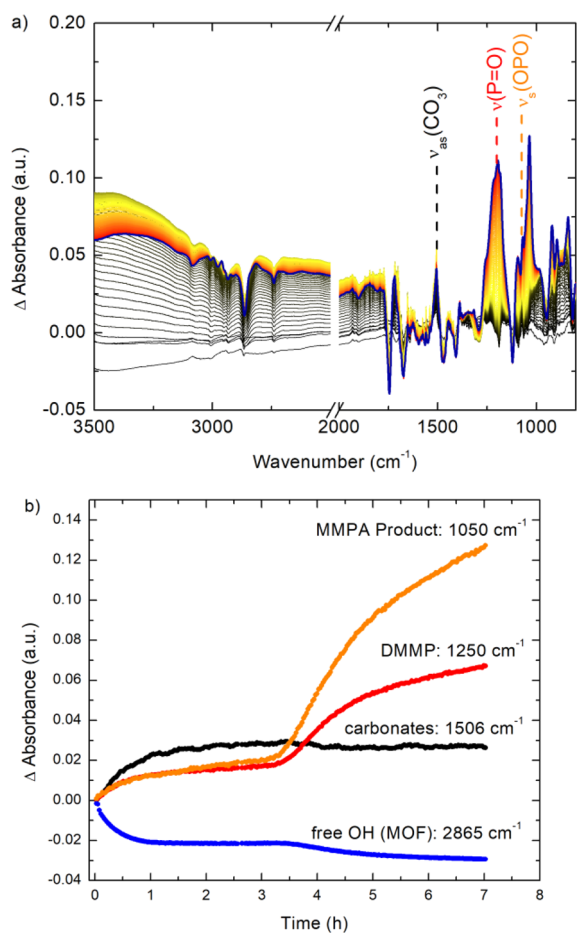

Figure 6. (a) In situ difference DRIFTS spectra collected over 7 h during a DMMP adsorption experiment with CO_2 carrier gas (flow rate 50 mL/min). (b) Evolution of the peak intensity of carbonate species $\nu_{as}(CO_3)$ and $\nu_s(OPO)$ from products of DMMP decompostion and $\nu(P{=}O)$ from physisorbed DMMP and free OH consumed during the reaction.

To confirm that the formation of carbonate species is linked to the presence of DMMP, we performed two control experiments, where MOF-808 was exposed to CO_2 and water. In the first experiment the gas mixture contained 10% H_2O and 20% CO_2 to more closely resemble real life conditions. In the second experiment the sample was saturated with CO_2 and then exposed to a He/H_2O mixture (100% relative humidity). In both cases, we observed the typical features induced by the adsorption of H_2O and CO_2 but no significant peak at ~1500 cm^{-1} was detected, indicating the absence of carbonate species (Figures S8–S13).

CO_2 Introduced after DMMP Loading as a Desorbant. An important challenge in developing reusable materials for next-generation filters is understanding desorption behavior. In the case of Zr-based MOFs, it has been previously established that DMMP decomposition leads to the formation of byproducts that irreversibly bind to under-coordinated Zr sites.[19] The experiments described above show that CO_2 interferes with the DMMP decompostion; therefore, we hypothesized that CO_2 can displace adsorbed DMMP. To verify this hypothesis, we performed two time-resolved DRIFTS desorption experiments using a N_2 and CO_2 gas flow at room temperature.

CO_2 introduction to DMMP-loaded MOF-808 leads to the formation of carbonate species, as evidenced by the appearance of the $\nu_{as}(CO_3)$ mode at 1506 cm^{-1}, similar to the experiment when both CO_2 and DMMP are introduced simultaneously (Figure S14). Further, after the gas flow is changed back to inert He, the prominent peak at 2336 cm^{-1}, consistent with physically sorbed gaseous CO_2, is still present, indicating that CO_2 interacts strongly with the DMMP-loaded MOF-808. The peak can only be removed by heating the sample to activation temperature (Figure S14).

In both N_2- and CO_2-driven desorption experiments after a 48 h gas flow at room temperature, the modes from adsorbed DMMP and bound MMPA are still present, indicating that without other means using only a gas flow for the regeneration of the MOF filter is not sufficient (Figure S15). However, after a closer look on the changing peak intensity, the modes from DMMP such as $\nu(P{=}O)$ at 1250 cm^{-1} lost intensity significantly in both the N_2 and CO_2 regimes, while modes from bound MMPA including $\nu_a(OPO)$ and $\nu_s(OPO)$ are less affected in N_2 than in CO_2 (Figure S14). Further, we analyzed the peak intensity change with time and we can see that CO_2 is increasing the rate of desorption of both DMMP and MMPA (Figure 7).

Computational Insights. To elucidate factors contributing to the influence of CO_2 on the DMMP decomposition by MOF-808, we turn to computational analysis. Previously, Troya, Morris, and co-workers[58] demonstrated by using the $Zr_6O_4(\mu_3\text{-}OH)_4(HCO_2)_{12}$ model of UiO-66 that CO_2 reversibly adsorbs onto UiO-66 (and possibly onto all MOFs in the Zr(IV)-MOF family) via both μ_3-OH groups located within the tetrahedral pores of the MOF and/or at the MOF surface with stabilizing hydrogen bonds and dispersion interactions, respectively. The reported bonding enthalpies, ΔH_{ads}, were −32.5 and −42.5 kJ/mol for dispersion-stabilized and hydrogen-bonded species, respectively, with −32.2 ± 1.8 kJ/mol enthalpy obtained by the VTIR experiments for the MOF-808 reported in this work. As could be expected, the value of the CO_2 absorption enthalpy depends on the MOF models adopted in the calculations. With computational analysis we obtained values of 21.8 and 27.3 kJ/mol CO_2 bonding enthalpy onto the μ_3-OH groups of the pristine $Zr_6O_4(\mu_3\text{-}OH)_4(HCO_2)_{12}$ and hydroxylated $Zr_6O_4(\mu_3\text{-}OH)_4(HCO_2)_{11}(OH)(H_2O)$ models, respectively. The examination of the calculated $(CO_2)/[MOF]$ structures (see Figure 8 and Figure S16) shows that CO_2 binds onto the μ_3-OH groups of MOF through a hydrogen bond, which was also reported previously.

Next, we examined the structural motif and energetics of the species formed upon simultaneous addition of MOF DMMP and CO_2 to MOF. As shown previously,[58] in the active form of MOF, the formate linkers are removed, which generates the
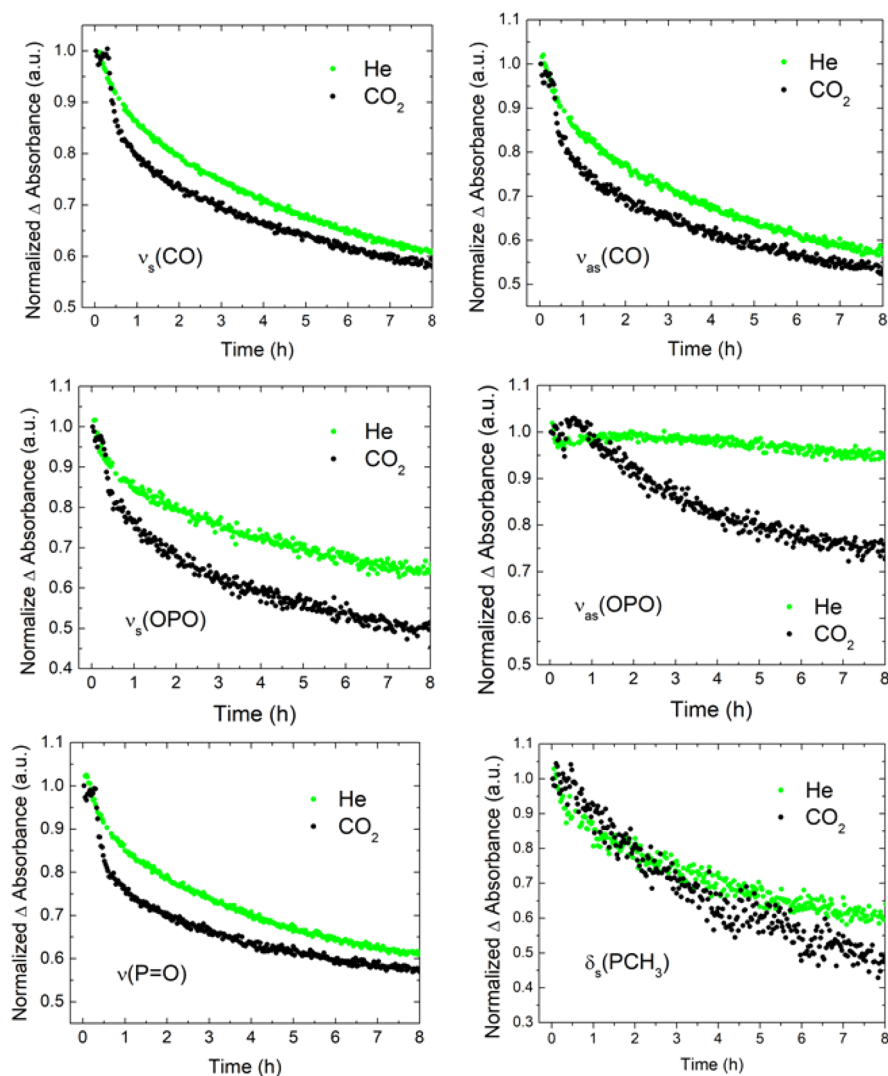
Figure 7. Time-resolved evolution of peak intensity from He and CO_2 desorption experiments.

active node with two adjacent coordinatively unsaturated Zr centers. One of these Zr centers is capped by a hydroxyl group, but another one is coordinated to a water ligand. In order for the DMMP hydrolysis to occur in this "hydroxyl-water" form of the MOF, the coordinated water molecule should be substituted by a DMMP molecule. Our calculations show that this water to DMMP substitution is almost a thermoneutral process (see Figure S17). The addition of the CO_2 molecule to the resultant $Zr_6O_4(\mu_3\text{-OH})_4(HCO_2)_{11}(OH)(DMMP)$ intermediate is found to be exothermic by 34.8 kJ/mol. A comparison of the CO_2 coordination enthalpies to $Zr_6O_4(\mu_3\text{-OH})_4(HCO_2)_{11}(OH)(H_2O)$ and $Zr_6O_4(\mu_3\text{-OH})_4(HCO_2)_{11}(OH)(DMMP)$, which are 27.3, and 34.8 kJ/mol, respectively, shows that DMMP coordination provides an additional stability to the $CO_2-(\mu_3\text{-OH})$ interaction. Since the DMMP hydrolysis directly involves the μ_3-OH group, as was revealed previously,[19] we expect that the additional $CO_2\text{---}(\mu_3\text{-OH})$ stabilization in the presence of DMMP hinders the DMMP decomposition. This conclusion is consistent with the DRIFTS experiments reported above indicating stronger CO_2 binding to the DMMP-loaded MOF-808 and lack of DMMP decomposition product until the completion of the carbonyl to carbonate transformation.

An additional support for this conclusion comes from the calculated thermodynamics of the involved elementary transformations $OH + CO_2 \rightarrow HOCO_2$ and $OH^- + CO_2 \rightarrow HOCO_2^-$, which are found to be exothermic (at the enthalpy level) by 33.9 and 298.8 kJ/mol, respectively.

Previous studies of DMMP decomposition by the Zr-based MOFs, in the absence of CO_2 gases, have revealed the formation of byproducts (MMPA) that strongly bind to the coordinatively unsaturated Zr centers.[19] Regeneration of the MOF catalyst requires removal of this byproduct (or its derivatives). As shown above, on the basis of the DRIFTS experiments, the addition of the CO_2 gas to the DMMP decomposition products alone is not sufficient for the regeneration of the MOF filter.

Consistent with this experimental observation, the presented calculations (Figure S16) show that CO_2 only weakly coordinates to the surface of the $Zr_6O_4(\mu_3\text{-OH})_4(HCO_2)_{11}(MMPA)$ through dispersive interactions. The calculated $CO_2-Zr_6O_4(\mu_3\text{-OH})_4(HCO_2)_{11}(MMPA)$ bonding enthalpy is 21.6 kJ/mol. However, the calculation also reveals that the presence of a water molecule in the reaction mixture may facilitate this process. Indeed, a water molecule binds slightly more strongly than CO_2 to $Zr_6O_4(\mu_3\text{-OH})_4(HCO_2)_{11}(MMPA)$, with 37.0 kJ/mol bonding enthalpy,
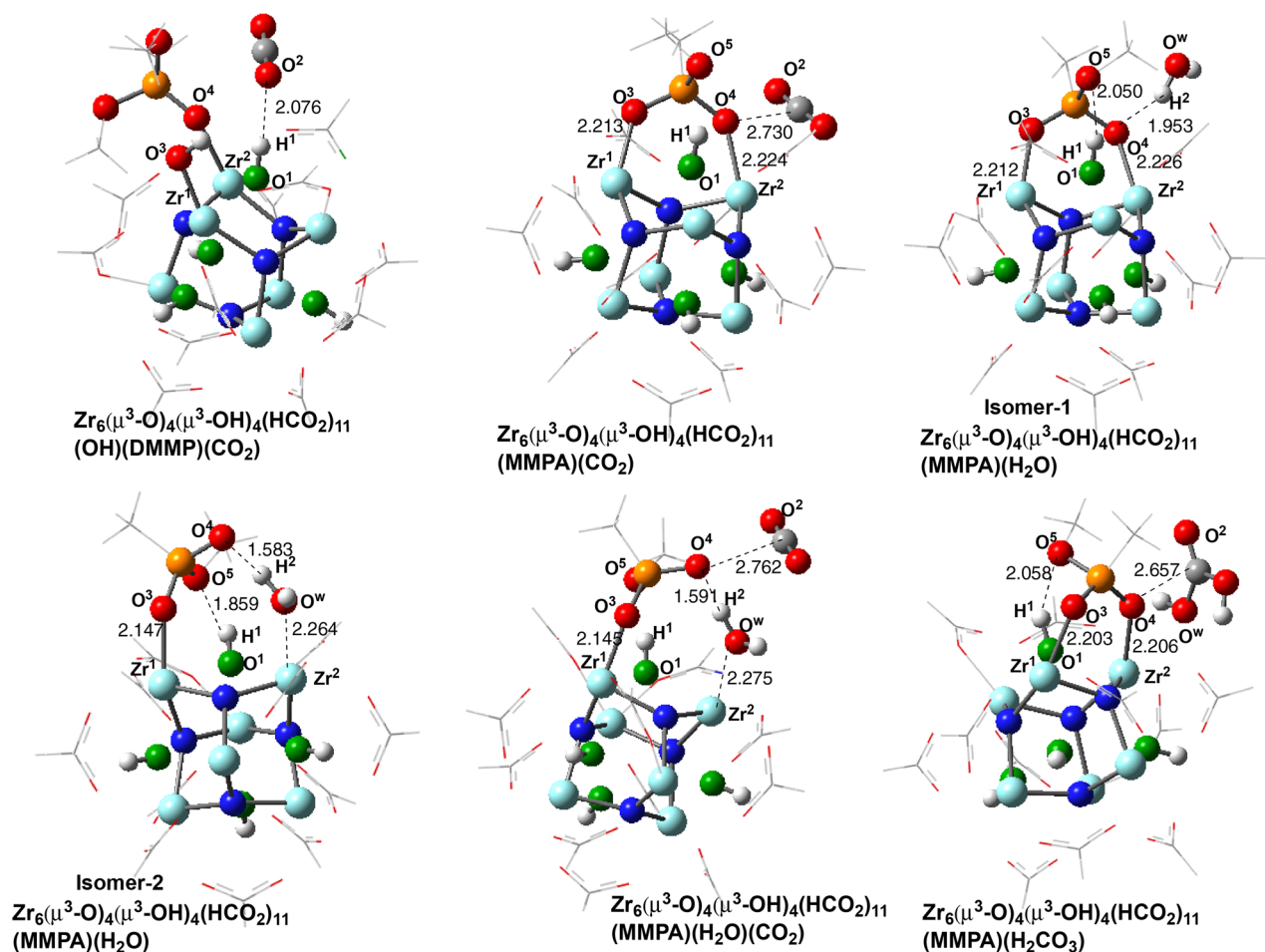
Figure 8. Calculated energetically lowest CO_2, H_2O, and H_2CO_2 complexes of various MOF-808 model systems used and discussed in this paper.

and could lead to carbonate formation and consequently to the facile removal of byproducts and regeration of the MOF filter (see Figure S16). This conclusion, on the basis of our limited computational data, is consistent with the experimental finding presented above which has shown that the presence of CO_2 increases the rate of desorption of both DMMP and MMPA. However, still more comprehensive computational and experimental studies are needed to reach more rigorous conclusions.

Thus, the computational data presented above show the following. (a) CO_2 reversibly adsorbs onto MOF-808 via both μ_3-OH groups located within the tetrahedral pores of the MOF and/or to the MOF surface with stabilizing hydrogen bonds and dispersion interactions, respectively. (b) The presence of DMMP provides an additional stabilization to the $CO_2-(\mu_3-OH)$ moiety, which hinders the μ_3-OH transfer to DMMP required for the nerve-agent decomposition. This conclusion is consistent with the findings from the DRIFTS experiments indicating no DMMP decomposition product until the completion of the carbonyl to carbonate transformation. (c) The addition of the CO_2 gas to the DMMP decomposition products alone is not sufficient for the regeneration of the MOF filter: the presence of a water molecule along with the CO_2 gas is required for the removal of DMMP decomposition byproducts and regeneration of the MOF filter.

CONCLUSIONS

In summary, we have studied the interaction between the Zr-based metal−organic framework MOF-808 and CO_2, as well as the influence of CO_2 on the absorption, decomposition, and desorption of DMMP, a sarin simulant. We established through variable-temperature infrared spectroscopy (VTIR) that CO_2 is adsorbed on the MOF with a relatively high energy of -32.2 ± 1.8 kJ/mol. In situ synchrotron X-ray diffraction results show that CO_2 is located inside the tetrahedral pores, presumably stabilized through dispersion interactions leading to the contraction of the framework volume by 0.2%. When CO_2 is introduced to MOF-808 together with DMMP, it leads to the formation of carbonate species, as evidenced from the growth of the $\nu_{as}(CO_3)$ mode at 1506 cm^{-1} observed in DRIFTS measurments. The reaction with CO_2 also hinders the decomposion of DMMP until the carbonate formation is complete. Introduction of N_2 together with DMMP leads to DMMP decomposition and formation of bound MMPA species, as observed before with He as a carrier gas.[33] Further, it was found that, when CO_2 is introduced after MOF-808 was saturated with DMMP, it also leads to formation of carbonate species as well as stronger binding of unreacted CO_2 molecules. The analysis of the kinetics of the reaction showed that CO_2 can accelerate the desorption of bound DMMP and decomposition of MMPA byproducts by reacting with bound MMPA. Our extensive computational analysis has provided an atomistic-level rationale to these important experimental findings.

■ ASSOCIATED CONTENT

ⓈSupporting Information

The Supporting Information is available free of charge at https://pubs.acs.org/doi/10.1021/acs.chemmater.9b04565.

Additional figures as detailed in the text (PDF)

■ AUTHOR INFORMATION

Corresponding Author
E-mail for A.I.F.: anatoly.frenkel@stonybrook.edu.
ORCID ⓘ
Anna M. Plonka: 0000-0003-2606-0477
Tyler G. Grissom: 0000-0001-7337-006X
Djamaladdin G. Musaev: 0000-0003-1160-6131
Yiyao Tian: 0000-0002-8148-9375
John R. Morris: 0000-0001-9140-5211
Anatoly I. Frenkel: 0000-0002-5451-1207

Notes

The authors declare no competing financial interest.

■ ACKNOWLEDGMENTS

■ REFERENCES

(1) Yang, Y. C.; Baker, J. A.; Ward, J. R. Decontamination of Chemical Warfare Agents. *Chem. Rev.* **1992**, *92*, 1729−1743.

(2) Koelle, G.; Compton, J. *Military Chemical and Biological Agents: Chemical and Toxicological Properties*; Telford Press: Caldwell, NJ, 1987.

(3) Kim, K.; Tsay, O. G.; Atwood, D. A.; Churchill, D. G. Destruction and Detection of Chemical Warfare Agents. *Chem. Rev.* **2011**, *111*, 5345−5403.

(4) Vorontsov, A. V.; Panchenko, A. A.; Savinov, E. N.; Lion, C.; Smirniotis, P. G. Photocatalytic Degradation of 2-Phenethyl-2-Chloroethyl Sulfide in Liquid and Gas Phases. *Environ. Sci. Technol.* **2002**, *36*, 5261−5269.

(5) National Research Council., *Review and Evaluation of Alternative Chemical Disposal Technologies*; National Academy Press: Washington, DC, 1996.

(6) Smith, B. M. Catalytic Methods for the Destruction of Chemical Warfare Agents under Ambient Conditions. *Chem. Soc. Rev.* **2008**, *37*, 470−478.

(7) Albright, R. *Cleanup of Chemical and Explosive Munitions*; William Andrew: Norwich, 2008.

(8) Wilcox, D. E. Binuclear Metallohydrolases. *Chem. Rev.* **1996**, *96*, 2435−2458.

(9) Kim, D. B.; Gweon, B.; Moon, S.; Choe, W. Decontamination of the Chemical Warfare Agent Simulant Dimethyl Methylphosphonate by Means of Large-Area Low-Temperature Atmospheric Pressure Plasma. *Curr. Appl. Phys.* **2009**, *9*, 1093−1096.

(10) Guo, W.; Lv, H.; Sullivan, K. P.; Gordon, W. O.; Balboa, A.; Wagner, G. W.; Musaev, D. G.; Bacsa, J.; Hill, C. L. Broad-Spectrum Liquid-and Gas-Phase Decontamination of Chemical Warfare Agents by One-Dimensional Heteropolyniobates. *Angew. Chem., Int. Ed.* **2016**, *55*, 7403−7407.

(11) Pastel, R. H.; Ritchie, E. C., Introduction to and Mitigation of Psychological Effects of Weapons of Mass Destruction (Wmd). In *Psychological Responses to the New Terrorism: a Nato-Russia Dialogue*; Wessely, S., Krasnov, V. N., Eds.; IOS Press, :Amsterdam, 2005; Vol. 3, pp 9−24.

(12) Wagner, G. W.; Peterson, G. W.; Mahle, J. J. Effect of Adsorbed Water and Surface Hydroxyls on the Hydrolysis of VX, GD, and HD on Titania Materials: The Development of Self-Decontaminating Paints. *Ind. Eng. Chem. Res.* **2012**, *51*, 3598−3603.

(13) Bandosz, T. J.; Laskoski, M.; Mahle, J.; Mogilevsky, G.; Peterson, G. W.; Rossin, J. A.; Wagner, G. W. Reactions of VX, GD, and HD with $Zr(OH)_4$: Near Instantaneous Decontamination of VX. *J. Phys. Chem. C* **2012**, *116*, 11606−11614.

(14) Collins-Wildman, D. L.; Kim, M.; Sullivan, K. P.; Plonka, A. M.; Frenkel, A. I.; Musaev, D. G.; Hill, C. L. Buffer-Induced Acceleration and Inhibition in Polyoxometalate-Catalyzed Organophosphorus Ester Hydrolysis. *ACS Catal.* **2018**, *8*, 7068−7076.

(15) Wang, Q.; Chapleski, R. C.; Plonka, A. M.; Gordon, W. O.; Guo, W.; Nguyen-Phan, T.-D.; Sharp, C. H.; Marinkovic, N. S.; Senanayake, S. D.; Morris, J. R.; Frenkel, A. I. Atomic-Level Structural Dynamics of Polyoxoniobates During DMMP Decomposition. *Sci. Rep.* **2017**, *7*, 773.

(16) Yang, S.-W.; Doetschman, D. C.; Schulte, J. T.; Sambur, J. B.; Kanyi, C. W.; Fox, J. D.; Kowenje, C. O.; Jones, B. R.; Sherma, N. D. Sodium X-Type Faujasite Zeolite Decomposition of Dimethyl Methylphosphonate (DMMP) to Methylphosphonate: Nucleophilic Zeolite Reactions I. *Microporous Mesoporous Mater.* **2006**, *92*, 56−60.

(17) Bromberg, L.; Schreuder-Gibson, H.; Creasy, W. R.; McGarvey, D. J.; Fry, R. A.; Hatton, T. A. Degradation of Chemical Warfare Agents by Reactive Polymers. *Ind. Eng. Chem. Res.* **2009**, *48*, 1650−1659.

(18) Islamoglu, T.; Ortuño, M. A.; Proussaloglou, E.; Howarth, A. J.; Vermeulen, N. A.; Atilgan, A.; Asiri, A. M.; Cramer, C. J.; Farha, O. K. Presence Versus Proximity: The Role of Pendant Amines in the Catalytic Hydrolysis of a Nerve Agent Simulant. *Angew. Chem., Int. Ed.* **2018**, *57*, 1949−1953.

(19) Wang, G.; Sharp, C.; Plonka, A.; Wang, Q.; Frenkel, A. I.; Guo, W.; Hill, C.; Smith, C.; Kollar, J.; Troya, D. Mechanism and Kinetics for Reaction of the Chemical Warfare Agent Simulant, DMMP (G), with Zirconium (IV) MOFs: An Ultrahigh-Vacuum and DFT Study. *J. Phys. Chem. C* **2017**, *121*, 11261−11272.

(20) Gil-San-Millan, R.; López-Maya, E.; Hall, M.; Padial, N. M.; Peterson, G. W.; DeCoste, J. B.; Rodríguez-Albelo, L. M.; Oltra, J. E.; Barea, E.; Navarro, J. A. Chemical Warfare Agents Detoxification Properties of Zirconium Metal−Organic Frameworks by Synergistic Incorporation of Nucleophilic and Basic Sites. *ACS Appl. Mater. Interfaces* **2017**, *9*, 23967−23973.

(21) de Koning, M. C.; van Grol, M.; Breijaert, T. Degradation of Paraoxon and the Chemical Warfare Agents VX, Tabun, and Soman by the Metal−Organic Frameworks UiO-66-NH₂, MOF-808, NU-1000, and PCN-777. *Inorg. Chem.* **2017**, *56*, 11804−11809.

(22) Momeni, M. R.; Cramer, C. J. Dual Role of Water in Heterogeneous Catalytic Hydrolysis of Sarin by Zirconium-Based Metal−Organic Frameworks. *ACS Appl. Mater. Interfaces* **2018**, *10*, 18435−18439.

(23) Chen, H.; Liao, P.; Mendonca, M. L.; Snurr, R. Q. Insights into Catalytic Hydrolysis of Organophosphate Warfare Agents by Metal−Organic Framework NU-1000. *J. Phys. Chem. C* **2018**, *122*, 12362−12368.

(24) Ryu, S. G.; Kim, M.-K.; Park, M.; Jang, S. O.; Kim, S. H.; Jung, H. Availability of Zr-Based MOFs for the Degradation of Nerve

Agents in All Humidity Conditions. *Microporous Mesoporous Mater.* **2019**, *274*, 9−16.

(25) Chen, Z.; Islamoglu, T.; Farha, O. K. Toward Base Heterogenization: A Zirconium Metal−Organic Framework/Dendrimer or Polymer Mixture for Rapid Hydrolysis of a Nerve-Agent Simulant. *ACS Appl. Nano Mater.* **2019**, *2*, 1005−1008.

(26) Yao, A.; Jiao, X.; Chen, D.; Li, C. Photothermally Enhanced Detoxification of Chemical Warfare Agent Simulants Using Bioinspired Core-Shell Dopamine-Melanin@ Metal-Organic Frameworks and Their Fabrics. *ACS Appl. Mater. Interfaces* **2019**, *11*, 7927−7935.

(27) Liang, H.; Yao, A.; Jiao, X.; Li, C.; Chen, D. Fast and Sustained Degradation of Chemical Warfare Agent Simulants Using Flexible Self-Supported Metal−Organic Framework Filters. *ACS Appl. Mater. Interfaces* **2018**, *10*, 20396−20403.

(28) Troya, D. Reaction Mechanism of Nerve-Agent Decomposition with Zr-Based Metal Organic Frameworks. *J. Phys. Chem. C* **2016**, *120*, 29312−29323.

(29) López-Maya, E.; Montoro, C.; Rodríguez-Albelo, L. M.; Aznar Cervantes, S. D.; Lozano-Pérez, A. A.; Cenís, J. L.; Barea, E.; Navarro, J. A. Textile/Metal−Organic-Framework Composites as Self-Detoxifying Filters for Chemical-Warfare Agents. *Angew. Chem., Int. Ed.* **2015**, *54*, 6790−6794.

(30) Mondal, S. S.; Holdt, H. J. Breaking Down Chemical Weapons by Metal−Organic Frameworks. *Angew. Chem., Int. Ed.* **2016**, *55*, 42−44.

(31) Mondloch, J. E.; Katz, M. J.; Isley, W. C., III; Ghosh, P.; Liao, P.; Bury, W.; Wagner, G. W.; Hall, M. G.; DeCoste, J. B.; Peterson, G. W. Destruction of Chemical Warfare Agents Using Metal−Organic Frameworks. *Nat. Mater.* **2015**, *14*, 512.

(32) Moon, S. Y.; Liu, Y.; Hupp, J. T.; Farha, O. K. Instantaneous Hydrolysis of Nerve-Agent Simulants with a Six-Connected Zirconium-Based Metal−Organic Framework. *Angew. Chem., Int. Ed.* **2015**, *54*, 6795−6799.

(33) Plonka, A. M.; Wang, Q.; Gordon, W. O.; Balboa, A.; Troya, D.; Guo, W.; Sharp, C. H.; Senanayake, S. D.; Morris, J. R.; Hill, C. L.; Frenkel, A. I. In Situ Probes of Capture and Decomposition of Chemical Warfare Agent Simulants by Zr-Based Metal Organic Frameworks. *J. Am. Chem. Soc.* **2017**, *139*, 599−602.

(34) Matito-Martos, I.; Moghadam, P. Z.; Li, A.; Colombo, V.; Navarro, J. A.; Calero, S.; Fairen-Jimenez, D. Discovery of an Optimal Porous Crystalline Material for the Capture of Chemical Warfare Agents. *Chem. Mater.* **2018**, *30*, 4571−4579.

(35) Sava Gallis, D. F.; Harvey, J. A.; Pearce, C. J.; Hall, M. G.; DeCoste, J. B.; Kinnan, M. K.; Greathouse, J. A. Efficient MOF-Based Degradation of Organophosphorus Compounds in Non-Aqueous Environments. *J. Mater. Chem. A* **2018**, *6*, 3038−3045.

(36) Liu, Y.; Howarth, A. J.; Vermeulen, N. A.; Moon, S.-Y.; Hupp, J. T.; Farha, O. K. Catalytic Degradation of Chemical Warfare Agents and Their Simulants by Metal-Organic Frameworks. *Coord. Chem. Rev.* **2017**, *346*, 101−111.

(37) Cho, K. H.; Chitale, S. K.; Kim, S.-J.; Cha, G.-Y.; Hong, D.-Y.; Ryu, S. G.; Chang, J.-S.; Hwang, Y. K. Adsorptive Removal of Nerve-Agent Simulant with Zirconium-Based Metal-Organic Frameworks Modified by Hydrophobic Monocarboxylic Acids. *Microporous Mesoporous Mater.* **2019**, *285*, 61−69.

(38) Li, B.; Wen, H. M.; Cui, Y.; Zhou, W.; Qian, G.; Chen, B. Emerging Multifunctional Metal−Organic Framework Materials. *Adv. Mater.* **2016**, *28*, 8819−8860.

(39) Sumida, K.; Rogow, D. L.; Mason, J. A.; McDonald, T. M.; Bloch, E. D.; Herm, Z. R.; Bae, T.-H.; Long, J. R. Carbon Dioxide Capture in Metal−Organic Frameworks. *Chem. Rev.* **2012**, *112*, 724−781.

(40) Banerjee, D.; Simon, C. M.; Plonka, A. M.; Motkuri, R. K.; Liu, J.; Chen, X.; Smit, B.; Parise, J. B.; Haranczyk, M.; Thallapally, P. K., Metal−Organic Framework with Optimally Selective Xenon Adsorption and Separation. *Nat. Commun.* **2016**, *7*, 11831.

(41) Huang, Y.-B.; Liang, J.; Wang, X.-S.; Cao, R. Multifunctional Metal−Organic Framework Catalysts: Synergistic Catalysis and Tandem Reactions. *Chem. Soc. Rev.* **2017**, *46*, 126−157.

(42) Chughtai, A. H.; Ahmad, N.; Younus, H. A.; Laypkov, A.; Verpoort, F. Metal−Organic Frameworks: Versatile Heterogeneous Catalysts for Efficient Catalytic Organic Transformations. *Chem. Soc. Rev.* **2015**, *44*, 6804−6849.

(43) Bobbitt, N. S.; Mendonca, M. L.; Howarth, A. J.; Islamoglu, T.; Hupp, J. T.; Farha, O. K.; Snurr, R. Q. Metal−Organic Frameworks for the Removal of Toxic Industrial Chemicals and Chemical Warfare Agents. *Chem. Soc. Rev.* **2017**, *46*, 3357−3385.

(44) Mondloch, J. E.; Bury, W.; Fairen-Jimenez, D.; Kwon, S.; DeMarco, E. J.; Weston, M. H.; Sarjeant, A. A.; Nguyen, S. T.; Stair, P. C.; Snurr, R. Q. Vapor-Phase Metalation by Atomic Layer Deposition in a Metal−Organic Framework. *J. Am. Chem. Soc.* **2013**, *135*, 10294−10297.

(45) Katz, M. J.; Moon, S.-Y.; Mondloch, J. E.; Beyzavi, M. H.; Stephenson, C. J.; Hupp, J. T.; Farha, O. K. Exploiting Parameter Space in MOFs: A 20-Fold Enhancement of Phosphate-Ester Hydrolysis with UiO-66-NH$_2$. *Chem. Sci.* **2015**, *6*, 2286−2291.

(46) Kalaj, M.; Palomba, J. M.; Bentz, K. C.; Cohen, S. M. Multiple Functional Groups in UiO-66 Improve Chemical Warfare Agent Simulant Degradation. *Chem. Commun.* **2019**, *55*, 5367−5370.

(47) Liu, Y.; Moon, S.-Y.; Hupp, J. T.; Farha, O. K. Dual-Function Metal−Organic Framework as a Versatile Catalyst for Detoxifying Chemical Warfare Agent Simulants. *ACS Nano* **2015**, *9*, 12358−12364.

(48) Balow, R. B.; Lundin, J. G.; Daniels, G. C.; Gordon, W. O.; McEntee, M.; Peterson, G. W.; Wynne, J. H.; Pehrsson, P. E. Environmental Effects on Zirconium Hydroxide Nanoparticles and Chemical Warfare Agent Decomposition: Implications of Atmospheric Water and Carbon Dioxide. *ACS Appl. Mater. Interfaces* **2017**, *9*, 39747−39757.

(49) Kaledin, A. L.; Driscoll, D. M.; Troya, D.; Collins-Wildman, D. L.; Hill, C. L.; Morris, J. R.; Musaev, D. G. Impact of Ambient Gases on the Mechanism of $[Cs_8Nb_6O_{19}]$-Promoted Nerve-Agent Decomposition. *Chem. Sci.* **2018**, *9*, 2147−2158.

(50) Furukawa, H.; Gándara, F.; Zhang, Y.-B.; Jiang, J.; Queen, W. L.; Hudson, M. R.; Yaghi, O. M. Water Adsorption in Porous Metal−Organic Frameworks and Related Materials. *J. Am. Chem. Soc.* **2014**, *136*, 4369−4381.

(51) Agrawal, M.; Sava Gallis, D. F.; Greathouse, J. A.; Sholl, D. S. How Useful Are Common Simulants of Chemical Warfare Agents at Predicting Adsorption Behavior? *J. Phys. Chem. C* **2018**, *122*, 26061−26069.

(52) Toby, B. H.; Von Dreele, R. B. Gsas-Ii: The Genesis of a Modern Open-Source All Purpose Crystallography Software Package. *J. Appl. Crystallogr.* **2013**, *46*, 544−549.

(53) Hammersley, A. Fit2d: An Introduction and Overview. *European Synchrotron Radiation Facility Internal Report ESRF97-HA02T*; 1997; p 68.

(54) Rietveld, H. A Profile Refinement Method for Nuclear and Magnetic Structures. *J. Appl. Crystallogr.* **1969**, *2*, 65−71.

(55) Petříček, V.; Dušek, M.; Palatinus, L. Crystallographic Computing System Jana2006: General Features. *Z. Kristallogr. Cryst. Mater.* **2014**, *229*, 345−352.

(56) Shearer, G. C.; Chavan, S.; Ethiraj, J.; Vitillo, J. G.; Svelle, S.; Olsbye, U.; Lamberti, C.; Bordiga, S.; Lillerud, K. P. Tuned to Perfection: Ironing out the Defects in Metal−Organic Framework UiO-66. *Chem. Mater.* **2014**, *26*, 4068−4071.

(57) Grissom, T. G.; Sharp, C. H.; Usov, P. M.; Troya, D.; Morris, A. J.; Morris, J. R. Benzene, Toluene, and Xylene Transport through UiO-66: Diffusion Rates, Energetics, and the Role of Hydrogen Bonding. *J. Phys. Chem. C* **2018**, *122*, 16060−16069.

(58) Grissom, T. G.; Driscoll, D. M.; Troya, D.; Sapienza, N. S.; Usov, P. M.; Morris, A. J.; Morris, J. R. Molecular-Level Insight into CO$_2$ Adsorption on the Zirconium-Based Metal-Organic Framework, UiO-66: A Combined Spectroscopic and Computational Approach. *J. Phys. Chem. C* **2019**, *123*, 13731−13738.

(59) Zhao, Y.; Truhlar, D. G. A New Local Density Functional for Main-Group Thermochemistry, Transition Metal Bonding, Thermochemical Kinetics, and Noncovalent Interactions. *J. Chem. Phys.* **2006**, *125*, 194101.

(60) Frisch, M., et al. *Gaussian09*; Gaussian, Inc.: Wallingford, CT, 2009.

(61) Hay, P. J.; Wadt, W. R. Ab Initio Effective Core Potentials for Molecular Calculations. Potentials for the Transition Metal Atoms Sc to Hg. *J. Chem. Phys.* **1985**, *82*, 270−283.

(62) Hay, P. J.; Wadt, W. R. Ab Initio Effective Core Potentials for Molecular Calculations. Potentials for K to Au Including the Outermost Core Orbitals. *J. Chem. Phys.* **1985**, *82*, 299−310.

(63) Garrone, E.; Areán, C. O. Variable Temperature Infrared Spectroscopy: A Convenient Tool for Studying the Thermodynamics of Weak Solid−Gas Interactions. *Chem. Soc. Rev.* **2005**, *34*, 846−857.

(64) Zhao, Z.; Li, Z.; Lin, Y. Adsorption and Diffusion of Carbon Dioxide on Metal−Organic Framework (MOF-5). *Ind. Eng. Chem. Res.* **2009**, *48*, 10015−10020.

(65) Plonka, A. M.; Banerjee, D.; Woerner, W. R.; Zhang, Z.; Nijem, N.; Chabal, Y. J.; Li, J.; Parise, J. B. Mechanism of Carbon Dioxide Adsorption in a Highly Selective Coordination Network Supported by Direct Structural Evidence. *Angew. Chem., Int. Ed.* **2013**, *52*, 1692−1695.

(66) Jiang, J.; Gándara, F.; Zhang, Y.-B.; Na, K.; Yaghi, O. M.; Klemperer, W. G. Superacidity in Sulfated Metal−Organic Framework-808. *J. Am. Chem. Soc.* **2014**, *136*, 12844−12847.

(67) Carrington, E. J.; Vitórica-Yrezábal, I. J.; Brammer, L. Crystallographic Studies of Gas Sorption in Metal−Organic Frameworks. *Acta Crystallogr., Sect. B: Struct. Sci., Cryst. Eng. Mater.* **2014**, *70*, 404−422.